ACI MATERIALS JOURNAL TECHNICAL PAPER

Title no. 107-M51

Bidirectional Multiple Cracking Tests on High-Performance Fiber-Reinforced Cementitious Composite Plates

by Benny Suryanto, Kohei Nagai, and Koichi Maekawa

An experimental program was conducted to investigate the effects of simultaneous opening-sliding of multiple cracks on the behavior of high-performance fiber-reinforced cementitious composites (HPFRCCs). For this purpose, 12 HPFRCC plates were tested in bending and under two constitutive principal stress directions. To facilitate reorientation of the stress fields, the plates were precracked and then sawn with certain orientations. Finally, the plates were retested in bending to failure. The results showed that the change in principal stress direction had a substantial effect on macroscopic plate behavior, as marked by reductions in strength and initial stiffness. The effect of stress field reorientation on the cracking pattern was, however, minimal. Regardless of the orientation of the new principal stress direction to that of precracking, a somewhat orthogonal crack pattern always appeared. To characterize the mechanisms involved, the stress-strain relationship within the constant moment span of each plate is presented and discussed.

Keywords: initial damage; multiple cracks; opening-sliding; strength degradation.

INTRODUCTION

High-performance fiber-reinforced cementitious composites (HPFRCCs) are a class of fiber-reinforced cement-based composites that exhibit multiple fine cracking and pseudo-strain hardening behavior in tension.[1-3] The focus of this paper is one material within the HPFRCC class called an engineered cementitious composite (ECC).[4] Basically, ECC is a fiber-reinforced mortar containing fine-graded materials[5] and a moderate amount (2 to 3%) of short random polymeric fibers.[4]

Since its first introduction in the early 1990s, ECC has gained increasing attention, particularly in situations where damage tolerance and crack-width control are of primary importance. Example applications of ECC include thin overlays (6 to 70 mm [0.25 to 3 in.]; Japan),[6] building dampers (steel-reinforced ECC [R/ECC] coupling beams for high-rise buildings; Japan),[6] bridge decks (R/ECC composite decks, 50 mm [2 in.] thick; Japan),[6] and bridge deck-link slabs (R/ECC link slabs; U.S.).[7,8]

To date, these advances in ECC use have largely benefitted from extensive research and experimentation over nearly two decades. In most cases, experiments with ECC have been conducted such that tensile/compressive stress was the major stress transferred across cracks. Li et al.[9] were among the first to point out the potential use of ECC in a shear intensive member after performing Ohno shear beam tests. Due to the biaxial stress state, multiple cracks, oriented normal to the principal tensile stress direction, first form at the center span of the beam. The beam finally fails in a ductile manner, resembling that of a reinforced concrete (RC) beam. Following this preliminary finding, further investigations have investigated the use of HPFRCC in enhancing the performance of various shear-critical members subjected to cyclic load reversal.[10-14] Under such reversed cyclic loading, an orthogonal crack pattern has commonly been observed. While cracks in one direction open, transferring tensile stress normal to the crack planes, the orthogonal cracks are in compression and, hence, close, and vice versa. To investigate the effects of alternate crack opening-closing more intensively, Kesner et al.[15] performed low-cycle tension-compression loading tests on small-scale specimens. They concluded that reversed cyclic loading has a negligible influence on the tensile response of HPFRCC unless peak compressive strength has been exceeded.

Much less attention has been paid to investigations of the performance of ECC with multi-directional cracking involving tensile and shear stress transfer across cracks and, at the same time, allowing some cracks to simultaneously open and slide. In fact, such crack kinematics may potentially occur under service-loading conditions, for instance, at a crack interface subjected to a complex stress condition such as in a bridge deck under moving loads or where an overlay material has cracked and is under the influence of surrounding damaged parts (refer to Fig. 1). In such conditions, not only may tensile stress develop at crack interfaces, but also shear stress. Adequate post-cracking shear resistance is thus required apart from superior post-cracking tensile resistance. Due to the absence of coarse aggregate, however, it is of concern that cracked ECC may possess little interface shear resistance, particularly when it

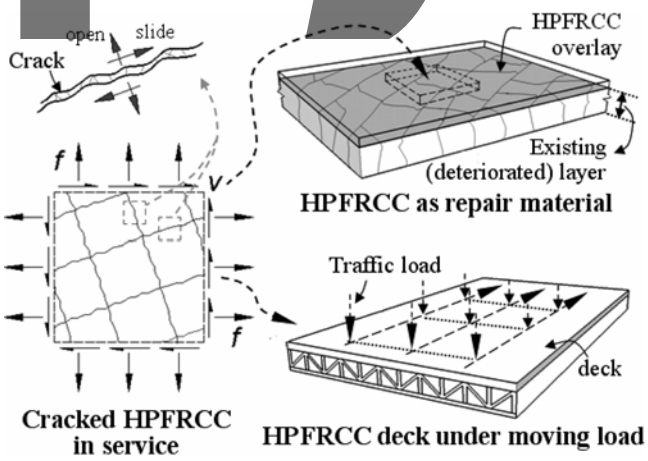

Fig. 1—Example of cracked HPFRCC in service situations.

ACI Materials Journal, V. 107, No. 5, September-October 2010.
MS No. M-2008-187.R2 received August 2, 2009, and reviewed under Institute publication policies. Pertinent discussion including authors' closure, if any, will be published in the July-August 2011 *ACI Materials Journal* if the discussion is received by April 1, 2011.

Benny Suryanto *is a PhD Student in the Department of Civil Engineering at the University of Tokyo, Tokyo, Japan. He received his BEng from Petra Christian University, Surabaya, Indonesia, in 2003 and his MEng from the Asian Institute of Technology, Bangkok, Thailand, in 2005. His research interests include the nonlinear mechanics of reinforced and fiber-reinforced concrete.*

Kohei Nagai *is an Assistant Professor in the Department of Civil Engineering at the University of Tokyo. He received his DEng in engineering from Hokkaido University, Saporro, Japan, in 2005. His research interests include the nonlinear mechanics of fiber-reinforced and reinforced concrete, and mesoscale discrete analysis of cementitious materials.*

Koichi Maekawa *is a Professor in the Department of Civil Engineering at the University of Tokyo. He received his DEng in engineering from the University of Tokyo in 1985. His research interests include the nonlinear mechanics of reinforced concrete, performance-based evaluation and life-span simulation of reinforced concrete structures, soil-structure interaction, and multiscale analysis of cementitious materials.*

is under repeated shear sliding. As a matter of fact, the newly constructed steel-ECC composite deck of the Mihara Bridge in Japan showed early signs of deterioration after only a few months of service,[16] with several localized and smooth cracks evident. This early deterioration is probably related to this issue, in addition to the snowball effect of water as already reported.[16]

This paper presents the results of an experimental program in which 12 precracked ECC plates were loaded in a four-point bending test; eight were tested under various levels and orientations of initial damage, while the rest were simply tested in bending. Various initial damage conditions were introduced to investigate the mechanisms of stress transfer across multiple cracks in cracked ECC. The macroscopic load-displacement, cracking characteristics, and average stress-strain behavior of the plates are presented and discussed. Particular attention is focused on the resulting secondary cracks (defined herein as a series of parallel cracks formed in a different orientation to the precracks).

RESEARCH SIGNIFICANCE

Previous research on the behavior of HPFRCCs has mainly focused on investigating performance involving tensile/compressive stress transfer across cracking. In actual service, however, HPFRCCs may inevitably be subjected to complex, nonproportional stress conditions that may result not only in tensile stress developed across cracks, but also shear stress. The present study, in which the direction of principal stress is changed, aims to highlight the importance of having a sufficient interface shear transfer in HPFRCCs.

EXPERIMENTAL PROGRAM

The experimental program involved the testing of 12 ECC plates produced in two batches. In each batch, there were two types of plate, namely control plates and main test plates. The control plates had dimensions of 400 x 250 x 20 mm (16 x 10 x 0.79 in.), whereas the main plates had dimensions of 550 x 420 x 20 mm (22 x 17 x 0.79 in.) (refer to Fig. 2(a)). The control plates served as a reference for the undamaged state, whereas the main plates were predamaged prior to main testing. An overview of the testing program is given in Table 1.

Preparation of specimens

A premixed polyvinyl acetate (PVA)-ECC material was used. The mixture proportion, as well as the mixing and casting procedures, is specified in Reference 17, whereas a brief summary of the mixture proportion is given in Table 2. Casting was done as specified in all cases. The average slump flow and air content of the material was

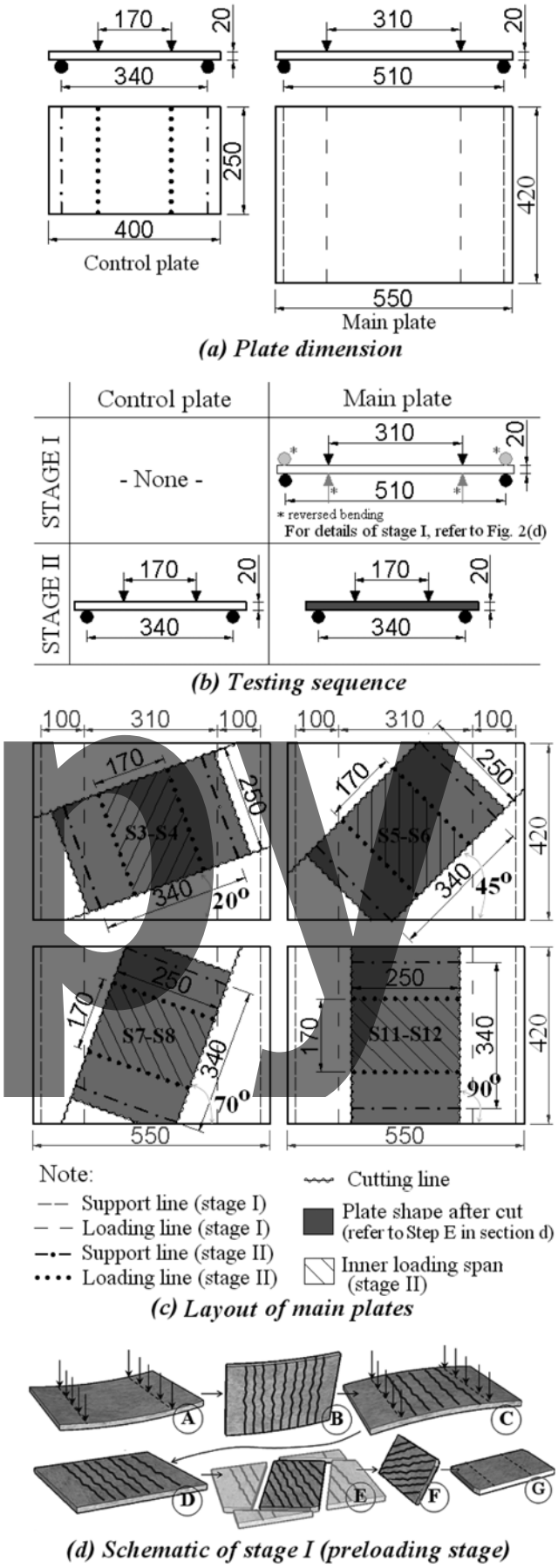

Fig. 2—Layouts and details of test plates. (Note: Dimensions in mm; 1 mm = 0.04 in.)

490 mm (19 in.) and 9%, respectively, for plates in the first batch and 510 mm (20 in.) and 15% for the second batch. After casting, all plates were fully covered with a plastic sheet and demolded after 2 days. Afterwards, the plates were air-cured in an ambient room with 60% relative humidity and a temperature of 20°C (68°F) until the test date (28 days after casting). The surface of the plates that had been at the bottom during casting was remarkably smooth and flat, whereas the upper surface was void rich. This void surface formation was particularly clearly observed in the case of specimens in the second batch. The size of the voids was approximately 0.1 to 0.5 mm (0.004 to 0.020 in.). For the first batch, the average compressive strength and modulus elasticity of the material were approximately 33 MPa and 15 GPa (4786.2 and 4,786,245.4 psi), respectively.

Testing procedure

To activate simultaneous crack-opening and crack-sliding mechanisms, a novel experimental technique was proposed. In essence, this technique recasts the widely known four-point bending test, but with a further advancement. Inspired by a testing technique previously implemented by Maekawa[18] and Van Mier,[19] the inclination of the principal stress direction was altered by cutting a larger, preloaded specimen. For this purpose, the course of the testing was divided into two testing stages: preloading (Stage I) and final loading (Stage II). The preloading stage (Stage I) was the damage initialization stage and was applied to the main plates only. Two experimental parameters were taken into account: damage level and damage orientation with respect to the damage of the plate soffit (refer to Table 1). The damage level parameter was set at two levels: low and high, corresponding to loading up to 40% and 70% of the average ultimate tensile strain of the control plates, respectively. For the second parameter, the plate was cut based on the layout given in Fig. 2(c), with four different orientations: 20, 45, 70, and 90 degrees. The final loading stage (Stage II) was the conventional four-point bending test and was applied to both control and main plates. Details of each testing stage are outlined in the following.

Table 1—Specimen details and experimental parameters

Batch	Plate ID	Dimensions W, mm (in.)	Dimensions L, mm (in.)	Dimensions H, mm (in.)	Initial damage Orientation, degree	Initial damage Level, % of ε_{tu}	Plate type
1	S1	250 (10)	400 (16)	20 (0.79)	—	—	Control
	S2				—	—	
	S3	420 (17)	550 (22)	20 (0.79)	20	40	Main
	S4				20	70	
	S5				45	40	
	S6				45	70	
	S7				70	40	
	S8				70	70	
2	S9	250 (10)	400 (16)	20 (0.79)	—	—	Control
	S10				—	—	
	S11	250 (10)	550 (22)	20 (0.79)	90	40	Main
	S12				90	70	

Note: — is no initial damage.

Table 2—Mixture proportion of PVA-ECC[17]

W/(C + FA), %	Water, kg/m^3 (lb/ft^3)	S/(C + FA), %	PVA fibers, % by volume
42.2	350 (22)	70	2.0

Note: W is water, C is ordinary portland cement, FA is fly ash, and S is sand. PVA fibers: diameter is 0.04 mm (0.0016 in.), length is 12 mm (0.47 in.), and tensile strength is 1600 MPa (232,000 psi).

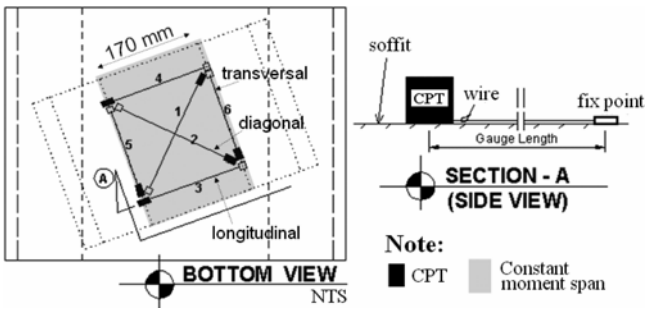

Fig. 3—Instrumentation showing soffit of Plate S3. (Note: Dimensions in mm; 1 mm = 0.04 in.)

Stage I: preloading stage

The complete procedure for the preloading stage is illustrated by letters A to F in Fig. 2(d). The plate was first loaded in a four-point bending test under the simply supported condition with a span of 510 mm (20 in.) (Step A). As loading proceeded, flexural cracks gradually formed at the plate soffit and propagated upwards. After reaching the target-damage level, the plate was unloaded and flipped (Step B). Reversed loading (Steps C and D) was then applied to return the plate to its original form prior to the final loading stage. As a result of this reversed loading, a few cracks were also observed at the top plate surface. This cracking might slightly reduce the initial stiffness of each plate during the final loading stage. Finally, the plate was cut (Step E) so as to align the cracks into the predefined orientation given in Table 1 and resize the plate to match the control plate. Given that there was no coarse aggregate in the plates, it was easy to make the cuts while preserving the preexisting cracks. At the end of the preloading stage, the plate was flipped again (Step F), making it ready for the final loading stage (Step G). At this stage, the plate soffit within the inner loading span can be regarded as a portion of a structure that has sustained cracking due to externally applied loads.

Stage II: final loading stage

The plate was placed in the simply supported condition with a span of 340 mm (13 in.). Displacement-controlled loading was then imposed on each quarter of the plate span in a monotonic manner until failure (refer to Fig. 2(b)). In all loading stages, displacement-controlled loading was applied at a rate of 0.5 mm (0.02 in.) per minute, using a 200 kN (45 kips) universal testing machine. These tests were carried out within 28 to 42 days after casting.

Instrumentation

Two types of transducer were used: the linear variable differential transducer (LVDT) and the miniature cable position transducer (CPT). Two LVDTs were mounted to the frame of the loading machine to obtain the average midspan deflection across the plate width, while six CPTs were attached to the plate soffit to obtain complete information on deformation of the soffit. The CPT is small (19 x 19 x 10 mm [0.75 x 0.75 x 0.38 in.]) and light (15 g [0.5 oz]); hence, it is very useful to

Table 3—Summary of experimental observations

Plate	Age, days	Achieved damage		Observed values					
		Orientation, degrees	Level, $\varepsilon_x/\varepsilon_{tu}$	P_u, kN (kips)	d_u, mm (in.)	Ratios of ultimate strain			
						$\varepsilon_x'/\varepsilon_{tu}$	$\varepsilon_x/\varepsilon_x'$	$\varepsilon_y/\varepsilon_x'$	$\gamma_{xy}/\varepsilon_x'$
S1	33	—	—	3.69 (0.83)	8.90 (0.35)	0.99	—	—	—
S2	33	—	—	3.76 (0.85)	9.12 (0.36)	1.01	—	—	—
S3	42	24	0.45	3.80 (0.85)	10.46 (0.41)	1.16	0.96	0.37	0.98
S4	39	21	0.70	3.60 (0.81)	10.24 (0.40)	1.33	1.27	0.22	0.80
S5	40	44	0.38	2.98 (0.67)	8.99 (0.35)	1.03	0.50	0.70	1.00
S6	35	35	0.72	3.25 (0.73)	11.38 (0.45)	1.27	0.82	0.52	1.30
S7	41	63	0.41	3.14 (0.71)	6.60 (0.26)	0.70	0.23	0.65	0.44
S8	38	68	0.71	2.57 (0.58)	10.48 (0.41)	1.12	0.45	0.97	0.78
S9	29	—	—	3.28 (0.74)	8.22 (0.32)	0.98	—	—	—
S10	29	—	—	3.56 (0.80)	8.58 (0.34)	1.02	—	—	—
S11	33	90	0.40	2.87 (0.65)	6.39 (0.25)	0.76	0.10	0.76	0.02
S12	32	88	0.74	2.99 (0.67)	7.87 (0.31)	0.99	0.11	0.99	0.08

Note: — is not applicable.

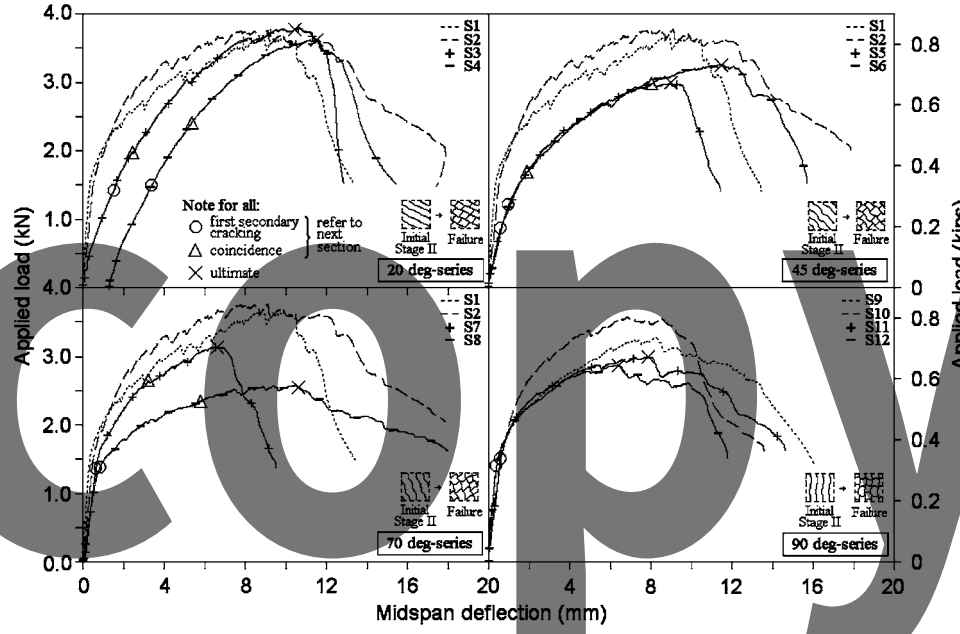

Fig. 4—Load-versus-midspan deflection of all plates. (Note: Dimensions in mm; 1 mm = 0.04 in.)

measure the apparent strain over an arbitrary gauge length spanning several cracks and on a convex surface. Figure 3 illustrates the configuration of the CPTs attached to the plate soffit: two longitudinal, two transversal, and two diagonal over the inner loading span of the main plate after cutting, forming a 170 mm (7 in.) square shape. The applied load acting on the test plates was identified using the load cell installed on the crosshead of the machine. All data were acquired at 1-second intervals. For the purpose of detailed crack observations, each plate soffit was treated with a fluorescent dye and then observed under fluorescent black lighting after testing.

MACROSCOPIC RESPONSE OF TESTED PLATES

The load-midspan deflection response of all plates is presented in Fig. 4; the dashed line corresponds to the results for the control plates (Plates S1, S2, S9, and S10), whereas the solid line represents those for the main plates (Plates S3 to S8, S11, and S12) during final loading (Stage II). Note that for Plate S4, measurements started with a permanent deflection of approximately 1.3 mm (0.05 in.) as, during the preloading stage, the loading head accidentally came into contact with the top plate surface. The ultimate load, its corresponding midspan deflection, and tensile strain, are summarized in Table 3. A schematic of initial cracking of the main plates prior to the second loading stage is illustrated in Fig. 5, whereas the corresponding crack pattern within the inner loading span after failure is depicted in Fig. 6.

Control plates (Plates S1, S2, S9, and S10)

The control plates exhibited ductile deflection hardening behavior far beyond initial cracking (refer to Fig. 4). As one would expect, this ductile behavior is due to the performance of PVA-ECC in tension. During this hardening response, a series of parallel cracks subsequently formed at the plate soffit (refer to Fig. 6 [Plates S1 and S2]). Most of the fluctuating response seen

in Fig. 4 can be attributed to this subsequent crack formation. Ductile response continued until some cracks were unable to bear the increasing tensile stress, became interconnected with each other, and ultimately formed one major localized crack across the plate soffit. The moment that this crack localized was the apparent time of maximum plate load. At that moment, the measurement of tensile strain at the plate soffit showed an average strain value of approximately 1.2% and 1.1% for the first batch plates (Plates S1 and S2) and second batch plates (Plates S9 and S10), respectively. These strain values were then used as reference values for determining the initial damage level of the main plates.

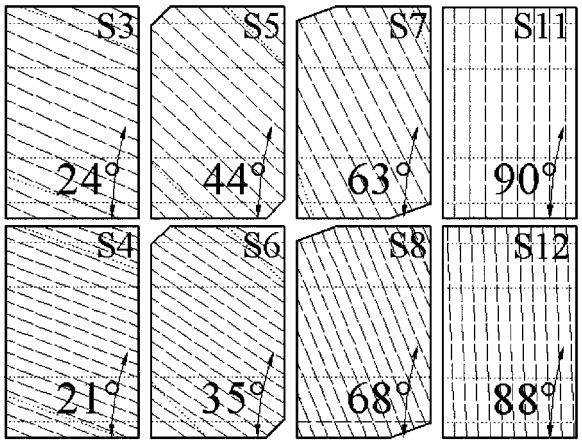

Fig. 5—Schematic of initial crack pattern.

Main plates (Plates S3 to S8, S11 and S12)

The first stage of testing (the preloading stage) resulted in well-established, uniform multiple cracks over the soffit of the main plates. Figure 5 illustrates the crack pattern observed on each main plate. For the first batch of plates designated for low initial damage conditions (Plates S3, S5, and S7) and high initial damage conditions (Plates S4, S6, and S8), the loading was terminated when the tensile strain reached approximately 0.5% and 0.9%, respectively. Accordingly, for the second batch of plates (Plates S11 and S12), it was terminated at approximately 0.4% and 0.7%, respectively. The predamage achieved in the main plates is summarized in Table 3.

During the second stage of testing (the final loading stage), it was observed that the main plates still behaved in a ductile manner, with a notable deflection-hardening response. The ductility of the main plates was not influenced by the preexisting multiple cracks; the only observation was a slight ductility reduction in Plates S5 and S7 (refer to Fig. 4). The precracks also had little influence on the cracking characteristics of the plates as indicated by the three typical cracking characteristics (refer to Fig. 6). First, cracking appeared in a bidirectional

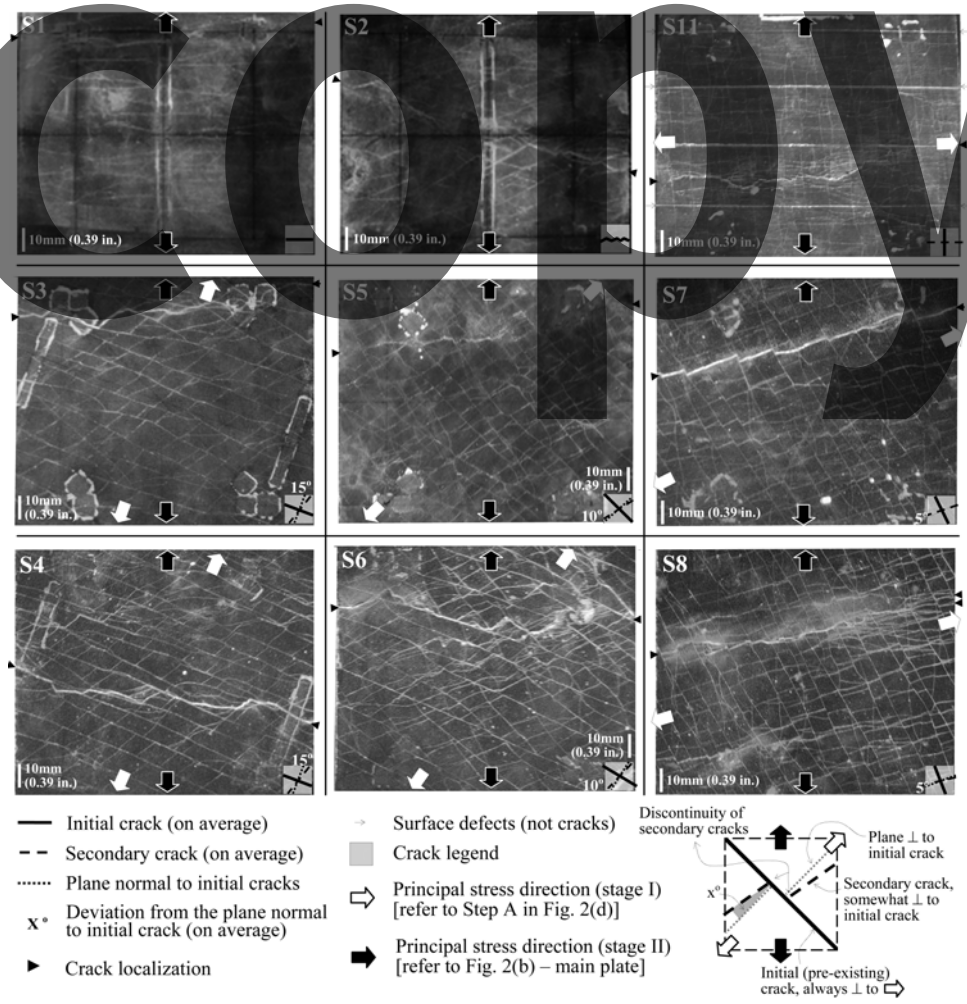

Fig. 6—Cracking pattern at plate soffit over inner loading span.

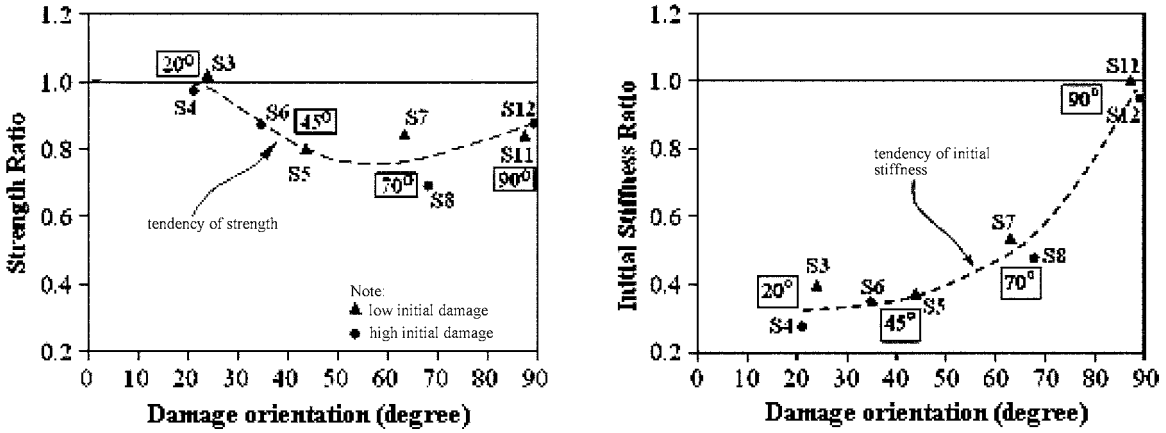

Fig. 7—Normalized strength and initial stiffness of main plates.

pattern, with initial cracks and then secondary cracks formed during the preloading and final loading stages, respectively. No premature failure was observed prior to formation of the secondary cracks. Second, initial cracks were uniform and continuous, whereas secondary cracks were visibly discontinuous. Both crack types were uniformly spaced between 5 and 15 mm (0.2 and 0.6 in.) apart. Third, the initial cracks were orthogonal to the principal stress direction of the preloading stage, whereas the secondary cracks always appeared near the orthogonal to the initial cracks, with variations of up to approximately 15 degrees. Interestingly, this angular variation appeared similar for each initial damage orientation—regardless of the damage level tested—with results of approximately 5, 10, and 15 degrees for the 70-, 45-, and 20-degree series of plates, respectively. The orthogonal crack pattern suggests that strong anisotropy is exhibited due to insufficient interface stress transfer along the precracks.

The failure mode of the plates was characterized by a typical discrete crack localization penetrating through the width of the plate adjoining the weakest preceding cracks (refer to Fig. 6). As can be seen from the figure, the location of this crack is also influenced by the orientation of the preexisting cracks. Crack localization in Plates S3 and S4 (the 20-degree cases) was more concentrated at the initial cracks, being adjoined by a few secondary cracks. Conversely, the crack localization in Plates S7, S8, S11, and S12 (the 70- and 90-degree cases) appeared at most of the secondary cracks. In Plates S5 and S6, the crack localization involved a more equal contribution of both initial and secondary cracks, suggesting the occurrence of more complex stress conditions.

The load-midspan displacement results shown in Fig. 4 indicate that the plate behavior was influenced by the existence of predamage. In general, the initial damage orientation tended to more adversely affect the plate response than did the degree of initial damage, in terms of initial stiffness and overall strength. The smaller the inclination of the damage orientation, the more significant the initial stiffness reduction. Conversely, the less significant was the decrease in strength. The first pair, Plates S3 and S4 (the 20-degree case), showed the largest reduction of initial stiffness (approximately 70%), but with no remarkable strength degradation. The second pair, Plates S5 and S6 (the 45-degree case), also showed some initial stiffness reduction (approximately 65%) as well as strength degradation (approximately 15%). The third pair, Plates S7 and S8 (the 70-degree case), experienced lower initial stiffness reduction (approximately 50%), but with the most severe strength degradation (approximately 25%). The last pair, Plates S11 and S12 (the 90-degree case), exhibited negligible initial stiffness reduction, but still showed a slight reduction of strength (approximately 10%).

For clarity, a summary of the strength and initial stiffness of the main plates tested under different damage orientations normalized by the values of the control plate is given in Fig. 7. It is apparent from Fig. 7(a) that no strength reduction occurred in Plates S3 and S4 (the 20-degree case), whereas the reduction in the other plates was approximately 10 to 30%. These differences can be explained by the fact that, in the 20-degree series, initial cracks were always subjected to more tensile stress than shear stress. Thus, the effect of shear slip was negligible and tension failure occurred along the precracks. As such, the influence of secondary cracks, which gradually formed somewhat orthogonal to the initial cracks, was less important. When transverse cracks exist from the beginning, such as in Plates S11 and S12 (the 90-degree case), this situation was found to cause a decrease in strength of approximately 10%. Thus, it seems possible that, in addition to the mechanism of opening and sliding at cracks, the preexisting transverse cracks may be another source of strength degradation in the other plate series (such as Plates S5 to S8). In other words, the greater the precrack angle, the more significant the weakening effects of the precracks. This weakening effect was notable in the 70-degree plates, where the precracks were almost parallel to the longitudinal plate direction and simultaneously opened and slipped. It is also evident from Fig. 7(b) that as the inclination of damage orientation becomes larger (up to 90 degrees), the initial stiffness reduction becomes less significant. This can be associated with a larger proportion of tensile stress resisted by the uncracked portions between the precracks.

AVERAGE STRESS AND STRAIN: SIMPLIFIED APPROACH

Stress-strain parallel and perpendicular to initial cracks

To characterize the underlying mechanism of the macroscopic response presented in the previous section, this section focuses on the average stress-strain behavior within the inner loading span. Because it was not possible to measure stresses directly from the occurring strains, this section presents an approximate stress-strain relation. It should be noted that cracked ECC under principal stress rotation behaves in a complex manner, with the involvement of stress-resisting mechanisms normal and parallel to the

existing cracks as well as the interface shear transfer. The behavior is even more complex after secondary cracks form. As such, a rigorous analysis procedure incorporating appropriate material models is required to relate stresses from the given strains. Because such a procedure has not yet been developed, a simplified analysis procedure is adopted on a tentative basis in this study according to the following strategy:

1. The stress-strain analysis is performed on a section within the inner loading span (refer to Fig. 8(a)) based on the assumption that plane sections remain plane. The adoption of this assumption leads to a linear variation of strain over plate depth as a function of the bottom fiber strain ε_t and curvature φ (refer to Fig. 8(b)) as follows

$$\varphi = \frac{\varepsilon_t}{d-x} = \frac{\varepsilon_c}{x} \tag{1}$$

2. To link the stress to the given longitudinal strain, two simple stress models are employed: a rigid-plastic model to represent the tension side and a linear model to represent the compression side (refer to Fig. 8(b)). Thus, the following two equilibrium expressions were adopted for analyzing the stress-strain relation of a section in the constant moment span

$$\sum F = 0$$
$$\frac{1}{2}E\left(\frac{\varepsilon_t}{d-x}\right)x^2 = f_t(d-x) \tag{2}$$

$$\sum M = 0$$
$$M = C\frac{2}{3}x + T\frac{1}{2}(d-x)$$
$$M = \frac{1}{3}\left(\frac{\varepsilon_t}{d-x}\right)Ebx^3 + \frac{1}{2}f_t b(d-x)^2 \tag{3}$$

Because E, d, and b are simply known, only four unknowns remain. Given the bottom fiber strain in the x' direction ε_t and the external moment acting on section M, the two equations can be solved for f_t and x.

3. Assuming that a two-dimensional stress state is dominant, the post-cracking response of ECC with respect to the orientation of an initial crack can be determined in three steps: first, a reference x-y coordinate is introduced, the x-axis of which is positioned along the opening direction of the initial crack; second, a x'-y' coordinate system is defined, the x'-axis of which is set along the principal stress direction in the final loading stage; third, both tensile stress f_t and strain ε_t are then transformed from the x' direction to the reference x-y coordinate system (refer to Fig. 8(c)).

Employing the first two strategies, the average ultimate tensile stress of the control plate f_{tu} was found to be approximately 3.6 and 3.4 MPa (522 and 493 psi) for plates of the first and the second batches, respectively.

The stress-strain behavior of the main plates with respect to the reference coordinate is presented in Fig. 9. Note that all of the stresses are normalized by the ultimate tensile stress of the control plate f_{tu}. It should also be noted that the stresses herein represent the average estimated stress values over a certain depth from the plate soffit, whereas the strains are the result of actual measurements at the plate soffit.

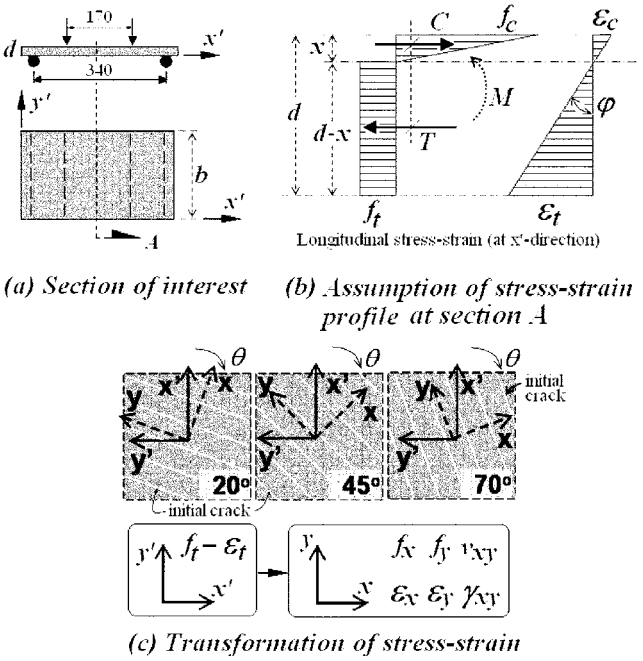

Fig. 8—Stress distribution calculation. (Note: 1 mm = 0.04 in.)

Apart from the stresses, discrete load data points are also provided in each plot in Fig. 9(a) so that one can also make use of the data for verification with a more refined stress-strain relation and a more advanced form of analytical modeling.

From the tensile stress-strain response normal to the initial cracks (refer to Fig. 9(a) through (c)), it is observed that ε_x is not zero at the beginning, although reversed loading had been applied, suggesting the presence of residual deformation. The onset of nonlinearity in the tensile stress-strain relationship parallel to the initial cracks f_y-ε_y (refer to Fig. 9(d) through (f)) indicates the onset of secondary cracking. Interestingly, despite the large variations of f_y at secondary cracking, a comparable normalized shear stress v_{xy} value is observed of approximately 0.14 (refer to Fig. 9(g) through (i)). This corresponds to a shear stress value of approximately 0.5 MPa (73 psi).

To describe the behavior of the plates prior to the onset of secondary cracking and, in particular, to explain the observed variations in macroscopic initial stiffness, shown in Fig. 7(b), the close-up of stress-strain behavior depicted in Fig. 9(j) through (l) is discussed. In general, it is found that the effect of damage orientation on the stress-strain behavior is significant. The greater the damage angle, the larger the contribution of uncracked parts between the preexisting cracks in resisting tensile stress. Hence, this results in a higher macroscopic initial stiffness. In the series of 20-degree plates, it is apparent that both opening ε_x and sliding γ_{xy} of initial cracks are more pronounced compared to deformation of the uncracked part ε_y (refer to Fig. 9(j)). Thus, the notable macroscopic initial stiffness decrease of this plate series can be exclusively attributed to the opening and sliding of initial cracks. In the 45-degree series of plates, it is evident from Fig. 9(k) that γ_{xy} is largest, followed closely by ε_y and ε_x, which are relatively constant. In contrast to the previous case, the reduction in initial stiffness in this plate series was mainly governed by the sliding of the precracks. In the 70-degree series, plate deformation involves both ε_y and γ_{xy}, while ε_x remains almost unchanged (or even falls slightly) (refer to

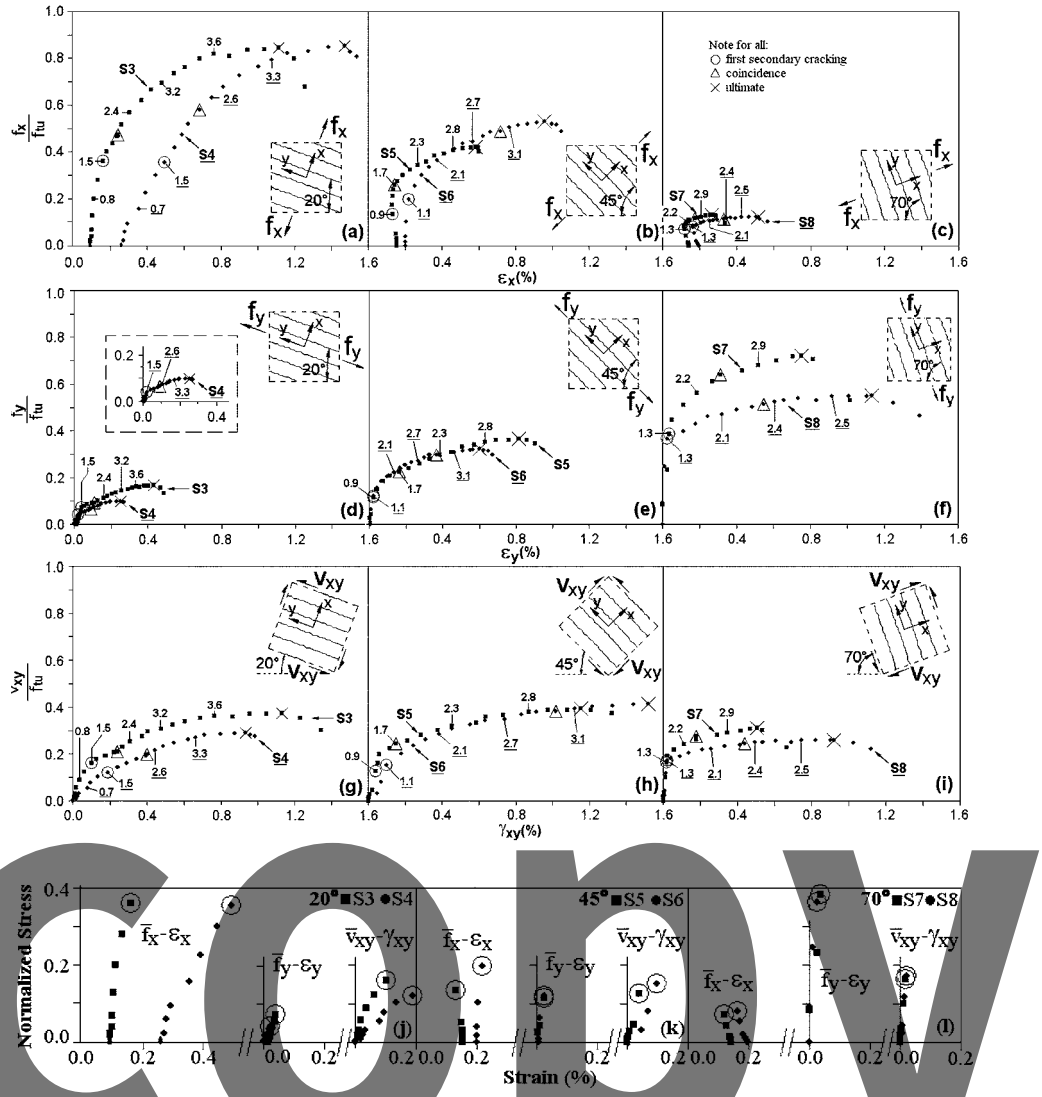

Fig. 9—(a) to (i) Assumed stress versus measured strain fields in x-y *coordinates (only initial crack orientations are shown in legend); and (j) to (l) close-up of stress-strain prior to first secondary cracking. (Note: Discrete numbers in Fig. 9(a) correspond to measured load value in kN; for kips multiply by 0.225.)*

Fig. 9(l)). It is obvious herein that as the uncracked part (the f_y-ε_y relationship) has acted as the main stress resisting mechanism, the macroscopic initial stiffness of the plates is much stiffer than those of the 20- and 45-degree series of plates.

The secondary cracks were formed mainly due to the tensile stress developed on the uncracked part itself and also due to the stress transferred by embedded fibers while crack-sliding takes place. Thus, not only did the tensile stress f_y dictate the initiation of secondary cracking, but also the shear stress v_{xy}. That is, v_{xy} is responsible for causing the deviation of the secondary cracks; the larger v_{xy}, the larger the deviation, given a similar f_y level. In the 20-degree plates, where the deviation was approximately 15 degrees, v_{xy} reached approximately twice f_y. For the plates in the 70-degree series, the magnitude of v_{xy} was similar but the f_y value was twice as high (relative to v_{xy}), and it is noticed that the deviation was approximately only 5 degrees. In the 45-degree plates with a 10-degree deviation, the two stresses were of comparable magnitude.

After secondary cracking, the deformation of the plate is more complex, particularly in the shear region as it includes the contribution of both initial and secondary cracks. Thus, further discussion is limited to a comparison of the stresses at failure. Figure 10 shows a two-dimensional projection from the actual three-dimensional tensile-shear interaction diagrams. For ease of comparison, all stresses have been normalized by the ultimate tensile stress f_{tu}. Rather than evaluating the stress values, it is of interest herein to investigate the difference between the two failure-envelope curves. The first curve (a polynomial fit) represents the ultimate tension-shear stresses of the test plates, whereas the second curve represents an ideal condition by assuming no strength reduction. As a result, the area between the two curves represents the strength degradation of the plates.

For the first diagram, a difference is visible between the two envelopes within the f_x range of 0.3 to 0.7 (refer to Fig. 10(a)). The effect of shear stress acting along the initial cracks is minor when the shear proportion is relatively small, such as in the case of both 20- and 70-degree series plates. For the second diagram, it is clear that the first curve is asymmetric (refer to Fig. 10(b)). The distance between the two curves can be interpreted as falling into the following four

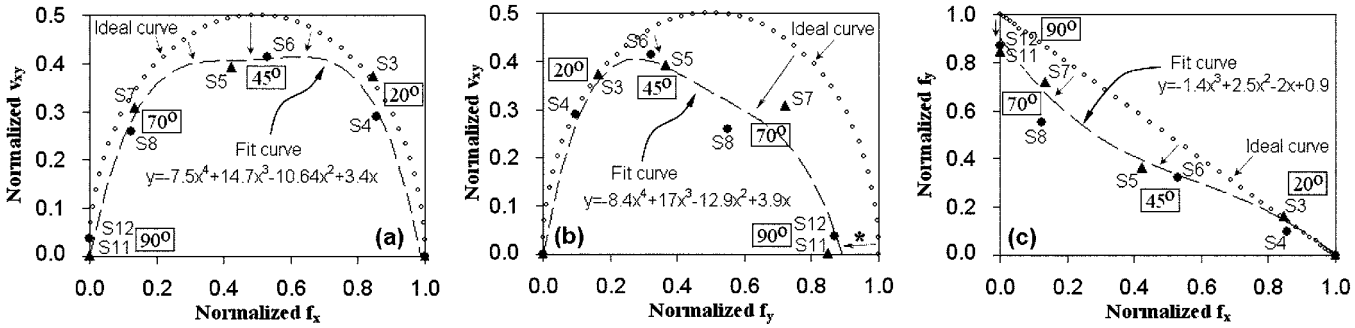

Fig. 10—Comparison of observed and ideal tensile-shear interaction diagrams of test plates.

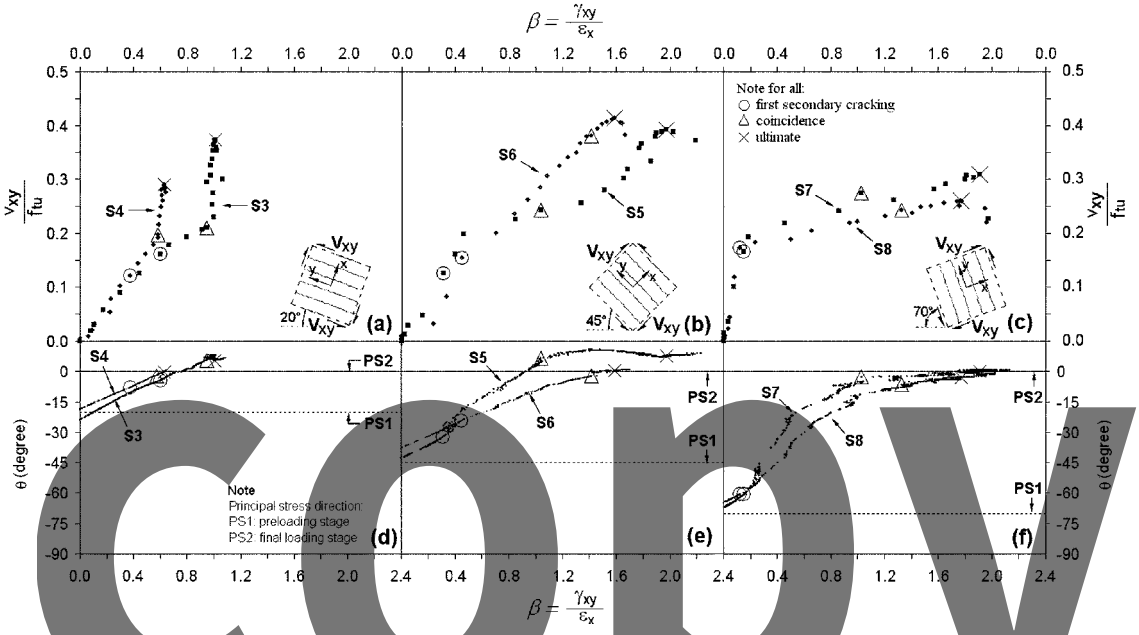

Fig. 11—Normalized shear stress and principal stress-strain direction versus β ratio.

categories. First, the distance from the 90-degree plates to the second curve (marked by * in the figure) can be attributed to the presence of the preexisting transverse cracks. The distance becomes larger in 70-degree plates, slightly smaller in 45-degree plates, and vanishes in 20-degree plates. Second, the fact that the difference is greatest for the 70-degree plates suggests that not only does a weakening effect of the preexisting transverse cracks exist (similar to the 90-degree plates), but so does a tensile-shear interaction. It should be noted, however, that the effect of the preexisting transverse cracks in this plate series should be less than that of the 90-degree series. Third, the distance in the case of the 45-degree series should correspond more strongly with the effect of tensile-shear interaction as the influence of transverse cracking should decrease to some extent herein. Fourth, there is almost no influence of either transverse cracking or tensile-shear interaction in the case of plates in the 20-degree series. Observation of the two diagrams reveals that the maximum shear stress is approximately 40% relative to the ultimate tensile strength. The third diagram (refer to Fig. 10(c)) shows a trend similar to the second.

Observed shear-transfer mechanism of multiple cracking

Crack kinematics incorporating the opening and sliding of a discrete crack have been successfully used to express shear transfer across cracked RC interfaces.[20,21] To obtain preliminary identification of interface shear transfer in ECC with multiple cracking, it is of interest, as well as being more convenient, to evaluate the average kinematics of multiple cracks, rather than the kinematics of every single crack. For this purpose, a parameter β is introduced, representing the ratio of average engineering shear strain γ_{xy} to average tensile strain ε_x. At first, this parameter is discussed together with the angle of the principal stress-strain direction to illustrate the apparent kinematics of the cracks. This parameter is then plotted together with the computed shear stress to gain insight into the shear-transfer mechanism of cracked ECC.

Observation of the principal stress-strain direction for various β-values shows that, at the very beginning of the final loading stage, the angle of principal strain coincided well with that of the principal stress direction at the preloading stage (Stage PS1) and lagged approximately 20, 45, or 70 degrees (depending on the orientation of the initial

damage) behind that of the principal stress of the final loading stage (Stage PS2) (refer to Fig. 11(d) through (f)). The coincidence of principal stress (Stage PS1) and strain suggests that, initially, only a crack-opening mechanism is operating. As loading proceeded, however, the preexisting cracks started to experience both crack-opening and crack-sliding behaviors as they were no longer perpendicular to the principal stress direction. Hence, the angle of the principal strain direction gradually shifted towards that of the current principal stress direction (Stage PS2), until eventually the two coincided (within 5 degrees). In an ideal case, principal stress and strain would completely coincide unless failure has commenced earlier. In reality, however, the inevitable presence of a slightly off-center position between the plate and test rig would lead to the slight deviation observed. The real coincidence can occur when the inclination of principal strain and stress are in close proximity to each other and, hence, it is difficult to be distinguished. Two events occurred when the inclination of the two almost coincided and were assumed as the first coincidence. The first event was marked by a relatively constant β value that remained unchanged until failure (refer to S3, S4, and S6 in Fig. 11(d) and (e)), whereas the second event was marked by an abrupt β increase.

The shear transfer of cracked ECC is shown in Fig. 11(a) through (c). Prior to the first secondary crack, shear stiffness is relatively linear. The shear stiffness varies from approximately 1.1 to 4.5 MPa (159 to 652 psi), with the largest values associated with the 70-degree series of plates. This finding suggests that crack-sliding is not exactly proportional to crack-opening; sliding tends to be more pronounced when the cracks reopen due to a higher f_x value, such as in the 20-degree plates (refer to Fig. 11(a)). When f_x is much lower than f_y and v_{xy}, such as in the 70-degree series, in which it was previously observed that the initial cracks closed slightly (Fig. 9(c)), the roughness of the crack itself may hinder slip and thereby decrease the β ratio.

After the first secondary crack, the influence of initial damage orientation is again of significance. In the 20-degree plates, the post-secondary-cracking shear stiffness is almost unchanged relative to the initial value (refer to Fig. 11(a)). This evidence suggests that the secondary cracks were not yet fully formed, thus leading to shear deformation still mainly governed by the sliding of initial cracks. Once the principal stress and strain coincide with each other, however, a much greater stiffness is observed, notably from a relatively constant β ratio of approximately 0.8 on average. This noteworthy increase in stiffness might be due to the simple opening-sliding of all cracks in the current principal stress direction (Stage PS2), considering that the β (strain) ratio is close to the engineering shear-to-tensile stress ratio ($2v_{xy}$ to f_x), which for 20-degree plates has a value of 0.75. On the other hand, the 70-degree series of plates show a notable reduction of shear stiffness after secondary cracking. It is likely that the abrupt opening of initial cracks after the first secondary crack, relative to the initial response (refer to Fig. 9 (c)), may lead the plate soffit to distort more easily, and thus increase the β ratio significantly (refer to Fig. 11 (c)). After the coincidence of principal stress and strain, no notable stiffness change is observed. Plates S5 and S6 (the 45-degree plate series) show a response that combines the behavior of the abovementioned plates (refer to Fig. 11(b)). Plate S5 exhibits a significant shear stiffness reduction after the first secondary crack, which is similar to the behavior of the 70-degree series of plates. At a later stage, a slight increase in the β ratio is observed, which is equivalent to that of the 20-degree plates. On the other hand, Plate S6, with an actual damage orientation of 35 degrees, shows a closer tendency to 20-degree plates at the early stage but with no increase of the β value at the later stage.

CONCLUSIONS

Twelve PVA-ECC plates were tested to investigate the influence of multiple cracks simultaneously opening and sliding with two test parameters: damage level (low and high) and damage orientation (20, 45, 70, and 90 degrees to plate longitudinal axis). As a reference for the undamaged state, four of the plates were designated as control plates. The observation of macroscopic plate behavior indicates that the damage orientation parameter is more dominant than the damage level parameter with respect to the observed strength and initial stiffness of the damaged plates. It is found that as the angle of the damage orientation becomes larger with respect to the longitudinal axis of the plate, there is an apparent strength reduction up to approximately 70 degrees and this then gradually falls when approaching 90 degrees while initial stiffness consistently increases with damage angle until it eventually reaches almost that of the control plate. Overall, the test results show that cracked PVA-ECC is an anisotropic material that exhibits behavioral changes depending on the orientation and extent of predamage.

The control plates exhibited a series of parallel cracks after loading, a typical cracking characteristic of ECC in tension or bending where the principal stress directions do not rotate. Once the ECC is precracked and subjected to principal stress rotation, three unique cracking characteristics were evident. First, cracking took place in a bidirectional pattern. Second, the initial cracks were uniform and continuous while the secondary cracks were discontinuous. Third, the orientation of the secondary cracks appeared close to orthogonal to the initial cracks with deviations up to 15 degrees. This rather orthogonal crack pattern, in particular, suggests the occurrence of a strongly anisotropic state owing to reduced interface stress transfer across crack surfaces.

Based on a simplified stress-strain assumption, the average stress-strain relation spanning multiple bidirectional cracks is developed and discussed. The orientation of the secondary cracks is shown to relate closely to the tensile and shear stresses arising at the precracks. A weakening effect due to transverse cracking was observed, in addition to the tensile-stress interaction problem. A preliminary indication of interface shear transfer in cracked ECC could also be derived. To better explain the underlying mechanism of precracked plates, work is currently underway on the development of a more refined stress-strain relation of cracked ECC and the incorporation of this relation into an analytical framework.

ACKNOWLEDGMENTS

The first author wishes to express his gratitude and appreciation to the Ministry of Education, Culture, Sports, Science and Technology, Japan, for the MEXT scholarship that enabled him to carry out this work. The authors are also thankful to Kajima Technical Research Institute for supplying the premix ECC material.

NOTATION

b = width of plate after cutting
d = depth of plate after cutting
d_u = midspan deflection at ultimate load
E = modulus of elasticity
f_t = tensile stress along x' direction on section within inner loading span

f_{tu} = ultimate tensile stress
f_x = assumed tensile stress normal to initial cracks
f_y = assumed tensile stress parallel to initial cracks
M = applied moment over inner loading span (constant moment span)
PS1 = principal tensile stress direction during preloading stage
PS2 = principal tensile stress direction during final loading stage
P_u = ultimate load
v_{xy} = assumed shear stress within 170 mm (6.69 in.) square region over inner loading span
x = depth of neutral axis from top edge
β = ratio of engineering shear to tensile strain
ε_c = top fiber strain over inner loading span along x' direction
ε_t = bottom fiber strain over inner loading span along x' direction
ε_{tu} = tensile strain of control plate at ultimate load
ε_x = tensile strain of plate soffit normal to initial cracks
ε_x' = tensile strain of plate soffit along principal stress direction during final loading stage
ε_y = tensile strain of plate soffit parallel to initial cracks
γ_{xy} = engineering shear strain of plate soffit within 170 mm (6.69 in.) square region over inner loading span
θ = alignment of principal stress and strain of main plates after cutting

REFERENCES

1. JCI-DFRCC Committee, "DFRCC Terminology and Application Concepts," *Journal of Advanced Concrete Technology*, V. 1, No. 3, 2003, pp. 335-340.

2. Naaman, A. E., "High-Performance Fiber-Reinforced Cement Composites," *Concrete Structures for the Future*, IABSE Symposium, Zurich, Switzerland, 1987, pp. 371-376.

3. Naaman, A. E., and Reinhardt, H. W., "Characterization of High Performance Fiber Reinforced Cement Composites—HPFRCC," *High Performance Fiber Reinforced Cement Composites 2 (HPFRCC 2)*, Proceedings of the Second International RILEM Workshop, A. E. Naaman and H. W. Reinhardt, eds., E&FN Spon, London, UK, 1996, pp. 1-24.

4. Li, V. C., "On Engineered Cementitious Composites (ECC)," *Journal of Advanced Concrete Technology*, V. 1, No. 3, 2003, pp. 215-230.

5. Sahraman, M.; Lachemi, M.; Hossain, K. M. A.; Ranade, R.; and Li, V. C., "Influence of Aggregate Type and Size on Ductility and Mechanical Properties of Engineered Cementitious Composites," *ACI Materials Journal*, V. 106, No. 3, May-June 2009, pp. 308-316.

6. Kunieda, M., and Rokugo, K., "Recent Progress on HPFRCC in Japan—Required Performance and Applications," *Journal of Advanced Concrete Technology*, V. 4, No. 1, 2006, pp. 19-33.

7. Li, V. C., and Lepech, M., "Crack Resistant Concrete Material for Transportation Construction," *Paper* No. 04-4680, 83rd Annual Meeting, Transportation Research Board, Washington, DC, 2004.

8. Li, V. C.; Lepech, M.; and Li, M., "Field Demonstration of Durable Link Slabs for Jointless Bridge Decks Based on Strain-Hardening Cementitious Composites," Michigan Department of Transportation *Research Report* No. RC-1471, 2005, 110 pp.

9. Li, V. C.; Mishra, D. K.; Naaman, A. E.; Wight, J. K.; LaFave, J. M.; Wu, H. C.; and Inada, Y., "On the Shear Behavior Of Engineered Cementitious Composites," *Journal of Advanced Cement Based Materials*, V. 1, No. 3, 1994, pp. 142-149.

10. Kesner, K., and Billington, S. L., "Experimental Response of Precast Infill Panels Made with DFRCC," *Proceedings of the JCI International Workshop on DFRCC*, Japan Concrete Institute, 2002, pp. 289-298.

11. Canbolat, B. A.; Parra-Montesinos, G. J.; and Wight, J. K., "Experimental Study on Seismic Behavior of High-Performance Fiber-Reinforced Cement Composite Coupling Beams," *ACI Structural Journal*, V. 102, No. 1, Jan.-Feb. 2005, pp. 159-166.

12. Parra-Montesinos, G. J., "High-Performance Fiber-Reinforced Cement Composites: An Alternative for Seismic Design of Structures," *ACI Structural Journal*, V. 102, No. 5, Sept.-Oct. 2005, pp. 668-675.

13. Kanda, T.; Watanabe, S.; and Li, V. C., "Application of Pseudo Strain Hardening Cementitious Composites to Shear Resistant Structural Elements," Proceedings FRAMCOS-3, AEDIFICATIO Publishers, Freiburg, Germany, 1998, pp. 1477-1490.

14. Fukuyama, H.; Sato, Y.; Li, V. C.; Matsuzaki, Y.; and Mihashi, H., "Ductile Engineered Cementitious Composite Elements for Seismic Structural Applications," *Proceedings of the 12th WCEE*, Paper No. 1672, 2000.

15. Kesner, K. E.; Billington, S. L.; and Douglas, K. S., "Cyclic Response of Highly Ductile Fiber-Reinforced Cement-Based Composites," *ACI Materials Journal*, V. 100, No. 5, Sept.-Oct. 2003, pp. 381-390.

16. Mitamura, H., "Development of a High-Performance, Economical ECC/Steel Plate Deck," *Report of Civil Engineering Research Institute for Cold Regions* No. 130, 2007, 197 pp. (in Japanese)

17. JSCE, "Recommendations for Design and Construction of High Performance Fiber Reinforced Cement Composite with Multiple Fine Cracks (HPFRCC)," *Concrete Library* 127, 2007, pp. 129-135. (in Japanese)

18. Maekawa, K., "Flow Rule and Plane Stress Constitutive Equations of Concrete," *Concrete Engineering*, V. 21, No. 8, 1983, pp. 103-121. (in Japanese)

19. Van Mier, J. G. M., "Influence of Damage Orientation Distribution on the Multiaxial Stress Strain Behavior of Concrete," *Cement and Concrete Research*, V. 15, 1985, pp. 849-862.

20. Li, B.; Maekawa, K.; and Okamura, H., "Contact Density Model for Shear Transfer Across Cracks in Concrete," *Journal of the Faculty of Engineering*, The University of Tokyo (B), V. XL, No. 1, 1989, pp. 9-52.

21. Bujadham, B.; Maekawa, K.; and Mishima, T., "The Universal Model for Stress Transfer Across Cracks in Concrete," *Proceeding of JSCE*, V. 17, No. 451, 1992, pp. 277-287.